An observing system simulation experiment (OSSE)-based assessment of the retrieval of above-cloud temperature and water vapor using hyperspectral infrared sounder

Jing Feng[1], Yi Huang[1], and Zhipeng Qu[1,2]

[1]Department of Atmospheric and Oceanic Sciences, McGill University
[2]Observations-Based Research Section, Environment and Climate Change Canada

Correspondence: Jing Feng (jing.feng3@mail.mcgill.ca)

Abstract. Measuring atmospheric conditions above convective storms is challenging. This study finds that the uncertainties in cloud properties near the top of deep convective clouds have a non-negligible impact on the TOA infrared radiances which cannot be fully eliminated by adopting a slab-cloud assumption. To overcome this issue, a synergetic retrieval method is developed. This method integrates the infrared hyperspectral observations with cloud measurements from active sensors to

5   retrieve atmospheric temperature, water vapor, and cloud properties simultaneously. Using an observation system simulation experiment (OSSE), we found that the retrieval method is capable of detecting the spatial distribution of temperature and humidity anomalies above convective storms and reducing the root-mean-square-errors in temperature and column integrated water vapor by more than half.

1 Introduction

10   Upper-troposphere and lower-stratosphere (UTLS) water vapor plays an essential role in controlling the outgoing longwave radiation (Huang et al., 2010; Dessler et al., 2013). It is argued to be a potential driver of surface climate change (Solomon et al., 2010) and to have important chemical effects (Shindell, 2001; Kirk-Davidoff et al., 1999; Anderson et al., 2012). Water vapor may enter the UTLS via two pathways: 1) through the slow ascent of the Brewer-Dobson circulation, and 2) through convective overshoots by transporting moist air or ice particles that sublimate in a warmer environment. While previous studies

15   (Anderson et al., 2012; Sun and Huang, 2015; Werner et al., 2020) have demonstrated the linkage between anomalously high water vapor concentrations and overshooting convections, the relative importance of deep convection to the UTLS water vapor budget is still under debate (Randel et al., 2015). To elucidate the problem, it is important to observe and understand the water vapor distributions above convective storms.

    While the knowledge of the UTLS composition has been contributed by aircraft in-situ measurements, it remains challenging

20   to sample air in extreme weather conditions near the top of storms. Satellite observational products have been extensively used to investigate the spatial and temporal variability of UTLS water vapor (Sun and Huang, 2015; Randel and Park, 2019; Yu et al., 2020; Wang and Jiang, 2019; Jiang et al., 2020). However, these products have a few limitations. First, above severe storms, the atmospheric profiles obtained by cloud-clearing retrieval schemes (Susskind et al., 2003; Gambacorta et al., 2014)

used by current hyperspectral infrared sounders are not reliable due to the overcast condition (Zhou et al., 2005). Second, for

25 limb-view and radio occultation instruments, the large sampling footprints limit the sensitivity of measurements to small-scale variations.

Recently, researchers have demonstrated the feasibility of single-footprint retrieval in cloudy-sky conditions by using simplified cloud parameters estimated from thermal radiances in the window channels (DeSouza-Machado et al., 2018; Feng and Huang, 2018). Feng and Huang (2018) found that observations from existing satellite hyperspectral infrared sounders,

30 such as AIRS (the atmospheric infrared sounder, Chahine et al., 2006), IASI (Infrared Atmospheric Sounding Interferometer, Blumstein et al., 2004) and CrIS (Cross-track Infrared Sounder, Bloom, 2001), contain substantial information content above optically thick upper-tropospheric clouds. They proposed a cloud-assisted retrieval technique and demonstrated that it is possible to detect both hydration and dehydration anomalies in the UTLS using infrared hyperspectra by validating their retrieval using aircraft observations. In these studies, the retrieval algorithm assumes that the upper-tropospheric clouds can be repre-

35 sented by a slab (thick and uniform layer) of ice clouds with fixed microphysics properties; a retrieval method following this assumption is referred to as slab-cloud retrieval in this paper.

However, neglecting the variability in cloud parameters, including cloud microphysical properties and the vertical distribution of ice content and temperature, may induce uncertainties in the spectral radiances. Yang et al. (2013) showed that the size and shape of ice particles have an impact on the scattering and absorption properties of ice clouds. Moreover, cloud emission

40 is important to the satellite-measured radiance at the TOA, because of weak infrared attenuation in the stratospheric column. Given the temperature lapse rate (Biondi et al., 2012) near the top of convective clouds, thermal emission from ice particles below the cloud top can be non-negligible to the satellite-measured radiance. Therefore, it is necessary to assess, and constrain, the impacts of these factors on retrieval accuracy.

On the other hand, the cloud uncertainties can be reduced by using collocated cloud data from active lidar or radar obser-

45 vations in the same satellite constellation as the hyperspectral infrared sounder. For example, the DARDAR-cloud (Delanoë and Hogan, 2008, 2010) product combines radar reflectivity measurements from CloudSat (Stephens et al., 2002) and lidar attenuated backscatter ratio from CALIPSO (Cloud-Aerosol Lidar and Infrared Pathfinder Satellite Observation, Winker et al., 2003) to provide ice water content (IWC) and effective radius profile, which can be integrated with the infrared hyperspectra from AIRS to form a synergetic UTLS retrieval.

50 Due to the lack of observations above storms, it is necessary to use an observing system simulation experiment (OSSE) to quantitatively evaluate the ability of such a synergetic retrieval and compare it to the slab-cloud method. In this study, we perform an OSSE based on the 'true' atmospheric conditions simulated by a high-resolution numerical weather prediction (NWP) model. This paper is structured as follows. The basic components of the OSSE, including the NWP model and radiative transfer model, are described in Section 2. We also discuss the radiance uncertainty induced by cloud microphysics properties

55 and vertical IWC distribution using the synthetic data with respect to both the slab-cloud and synergetic methods. In section 3, a quantitative evaluation of the retrieval of UTLS temperature, humidity, and IWC is performed. The application of the improved synergetic-cloud retrieval scheme to the existing instruments is discussed in Section 4.

2   Method

The OSSE in this study consists of the following components:

60   1. a cloud-resolving NWP model, which is used to provide the 'Truth' of atmospheric conditions during a tropical cyclone event, as described in Section 2.1;

2. a radiative transfer model, which is used as a forward model in the retrieval and to generate synthetic infrared hyperspectra with the instrument specifications of AIRS, as described in Section 2.2;

3. retrieval algorithms as explained in Section 2.3; and

65   4. comparisons between the retrieved quantities and the Truth in Section 3.

2.1   Numerical weather prediction model

In this study, we use the Global Environmental Multiscale model (GEM) of Environment and Climate Change Canada (hereafter ECCC, Côté et al., 1998; Girard et al., 2014) to provide a detailed and realistic representation of storm-impacted atmospheric and cloud profiles, following the study of Qu et al. (2020). The GEM model is formulated with non-hydrostatic
70   primitive equations with a terrain-following hybrid vertical grid. It can be run as a global model or a limited-area model and is capable of one-way self-nesting. For the experiments conducted here, three self-nested domains are used with areas of $3300{\times}3300$, $2000{\times}2000$, and $1024{\times}1024$ km^2 and horizontal grid-spacings of 10, 2.5, and 1 km, respectively, centered in a tropical Pacific region. All simulations use 67 vertical levels, with vertical grid-spacing $\Delta z{\approx}250$ m in the UTLS region and a model top at 13 hPa. The simulation is initialized with conditions from the ECCC global atmospheric analysis at 00:00 UTC
75   16 May 2015. It runs for 24 hours until 00:00 UTC 17 May 2015. Model outputs at 1 km horizontal grid-spacing are saved every 10 minutes and used in the OSSE.

For the two high-resolution simulations with 2.5 and 1 km horizontal grid-spacing, the double-moment version of the bulk cloud microphysics scheme of Milbrandt and Yau (2010a, b; hereinafter referred to as MY2) is used. This scheme predicts the mass and number mixing ratio for each of six hydrometeors including non-precipitating liquid droplets, ice crystals, rain, snow,
80   graupel, and hail. Condensation (ice nucleation) is formed only upon reaching grid-scale supersaturation with respect to liquid (ice). In addition to the MY2 scheme, the planetary boundary-layer scheme (Bélair et al., 2005) and the shallow convection scheme (Bélair et al., 2005) can also produce cumulus, stratocumulus, and other low-level clouds, which are of less relevance to our UTLS-centric OSSE.

A snapshot from the 1-km resolution GEM simulation, 410 minutes after the initial time step, is used for the radiance
85   simulation, because the storm matures and then generates abundant samples suitable for the retrieval at this time. Figure 1 shows the atmospheric conditions at this time step, including the distributions of temperature and water vapor at 81 hPa, at which level the variance is the largest. The distribution of the simulated cloud field is indicated by BT_{1231}, the brightness temperature in a window channel at 1231 cm^{-1}, simulated by a radiative transfer model (see the description below). A cold BT_{1231} suggests a deep convective cloud (DCC) that extends to the tropopause level. Overshooting DCCs are identified based

90   on the BT difference between a water vapor channel (BT_{1419} cm^{-1} at 7.0 μm) and BT_{1231} (8.1 μm, Aumann and Ruzmaikin, 2013). 9941 overshooting DCC profiles are identified using this criterion, their locations are marked in Figure 1. From the GEM outputs, these profiles are confirmed to be precipitating, with continuous clouds extending from near-ground to vertical levels above 120 hPa, the level of tropopause. We use the BT-based criterion to select retrieval locations, instead of examining GEM-simulated cloud and precipitation fields, to mimic the scenario of using infrared radiance measurements only to identify

95   overshooting DCCs, as performed in Feng and Huang (2018). Among the identified overshooting clouds, 100 profiles are randomly selected to construct a test set. The size of the samples is verified to meet the convergence requirement of the statistical evaluation conducted in Section 3. The rest of simulation profiles, in the number of O(10^6), regardless of cloud conditions, are used to construct an *a priori* dataset to define the prior knowledge used in the retrieval in Section 2.3.

2.2   Radiative transfer model

100   This study uses the MODerate spectral resolution TRANsmittance, version 6.0 (MODTRAN 6.0) (Berk et al., 2014) to simulate the infrared radiances observed by satellite. MODTRAN 6.0 provides a line-by-line (LBL) algorithm that calculates radiance at 0.1 cm^{-1} spectral steps. This algorithm is validated against a benchmark radiation model, LBLRTM, showing less than 0.005 differences in atmospheric transmittance throughout most of the spectrum (Berk and Hawes, 2017). MODTRAN 6.0 implements a spherical refractive geometry package and the DISORT discrete ordinate model to solve the radiative transfer

105   equation accounting for both absorptive and scattering media in the atmosphere (Berk and Hawes, 2017).

In this study, we use MODTRAN 6.0 to simulate the all-sky radiances with user-defined atmospheric profiles including cloud information. The model has 80 fixed atmospheric pressure levels. Above the GEM model top, the values from a standard tropical profile (McClatchey, 1972) are placed between 13 and 0.1 hPa. The prescription of the cloud information is based on an optical library of Yang et al. (2013). The cloud optical library provides a look-up table for the single-scattering properties

110   of ice particles of different habit shapes, roughness, and sizes. Following Bani Shahabadi et al. (2016), we assume a gamma distribution of particle sizes and calculate the single-scattering properties of each ice habit for the effective radius range between 1 to 100 μm. The effect of effective radius and ice habit on the simulated infrared radiance is discussed in Section 2.2.1, over the spectral ranges from 200 to 2700 cm^{-1}. Liquid clouds at lower levels are neglected because their infrared emissions are completely attenuated by ice clouds in the DCC samples concerned here.

115   In this OSSE, to mimic the retrieval using existing measurements, we follow the instrument specifications of AIRS, an infrared hyperspectral infrared sounder onboard the Aqua satellite since 2002. This instrument has 2378 channels from 650 to 2665 cm^{-1} with a noise equivalent temperature difference (NEdT) around 0.3 K (at 250K reference level). Using AIRS spectral response function, synthetic radiances are generated using MODTRAN 6.0 from the atmospheric profiles of the GEM test set described above, and then are added with random, spectrally uncorrelated noise based on the NEdT of AIRS. These

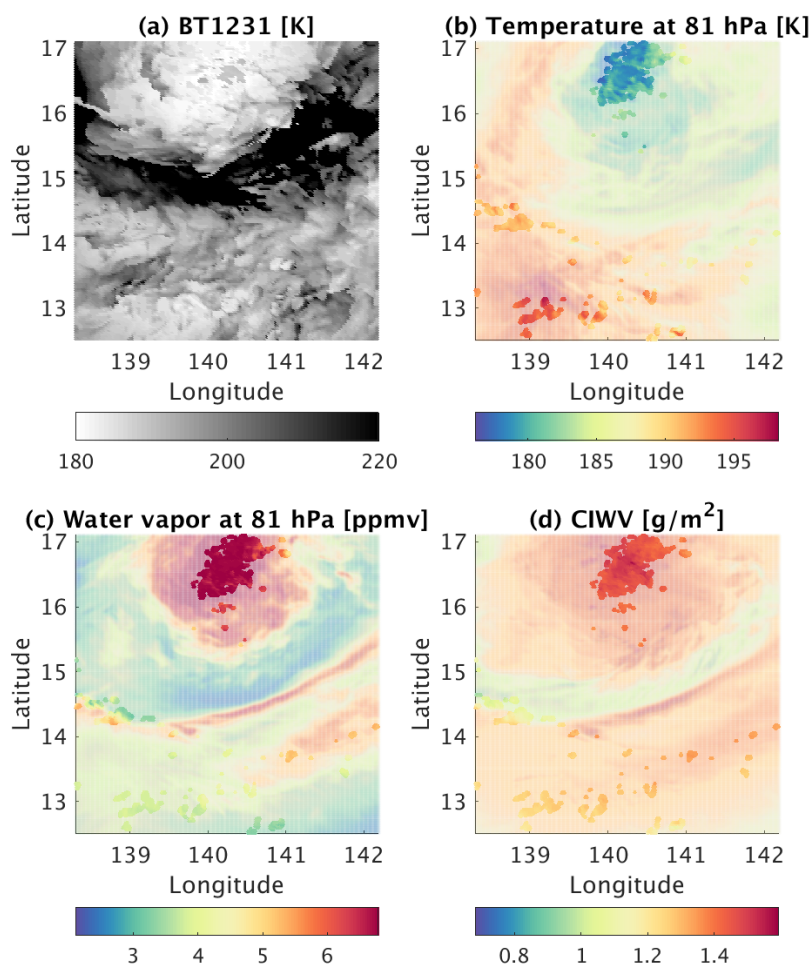120   infrared radiance spectra are used as the simulated observations in the OSSE.

Figure 1. GEM-simulated atmospheric conditions used as the "Truth" in the OSSE. (a) Brightness temperature [K] of upwelling radiances at TOA at 1231 cm-1. (b) Temperature [K] at 81 hPa. (c) Water vapor volume mixing ratio [ppmv] at 81 hPa. (d) Column integrated water vapor (CIWV) from 110 to 70 hPa. Solid color-coded dots mark the locations of deep convective clouds from which the test set is sampled to conduct the retrievals; in transparent colors are the rest of simulated fields. The variable fields are taken at 410 minutes after the initial time step.

Atmospheric
Measurement
Techniques
Discussions

2.2.1 Cloud induced uncertainties

In the following, we evaluate the radiance variability that results from 1) the variability in cloud microphysics properties, especially the effective radius of ice particles, and 2) the variability in the vertical distribution of the IWC profile. The surface roughness of ice particles is neglected as it mainly affects the scattering angle which plays a minor role in the infrared channels. We focus on tropical cyclone events for their relevance to the OSSE case here.

To gain the knowledge of cloud ice particles and their impacts on the infrared radiance spectrum and also to prescribe relevant information in the UTLS retrieval (see the descriptions below), DARDAR-cloud, a synergic lidar-radar retrieval product, is sampled to form a cyclone overpasses dataset based on the CloudSat 2D-TC data (Tourville et al., 2015). This overpass dataset identifies satellite overpasses within 1000km from the cyclone centers. From these overpasses, profiles with overshooting DCCs above 16km altitude (OT-DCC) are selected from 947 cyclones in the western part of the Pacific from 2006 to 2016. A total number of 98293 profiles are identified, which consists of IWC and effective radius at a vertical resolution of 60 m.

First, based on the identified OT-DCC profiles, we calculate the probability distribution function of the effective radius of ice particles at the cloud top. Fig .2 shows that the ice particles are typically small, with an average effective radius of 21.5 μm and the 1st and 99th percentiles of 13.3 and 39.7 μm respectively. According to Heymsfield (1986) and Baum et al. (2011), over 80% of the small ice particles at tropical high-altitudes are solid columns. Hence, in the following, we consider the ice particles to be solid column only, with a rough surface but varying effective radius.

Then, we randomly select 100 profiles from identified OT-DCCs to evaluate the effects of varying IWC and effective radius on the infrared radiance spectra. We calculate the upwelling infrared radiances $R(Re, IWC_0)$ using IWC_0, the mean IWC of OT-DCCs, and effective radius Re of every profile. Fig. 3 (a) shows the mean and the standard deviation (STD) of the equivalent brightness temperature of $R(Re, IWC_0)$ caused by effective radius variations. Similarly, the mean and STD of $R(Re_0, IWC)$ caused by IWC variations are shown in Fig. 3 (b). Note that a 0.1 cm^{-1} spectral resolution is used in radiative transfer calculation for this evaluation.

As shown in Fig.3 (a,b), the mean spectra of OT-DCCs show cold, and relatively uniform, brightness temperatures in the window and weak absorption channels that largely result from the emission of the cloud top. While the varying effective radius and IWC have a weak effect on the strong absorption channels, it greatly impacts the cloud emission, thus leading to large radiance variations in the window and weak absorption channels. In the mid-infrared, the standard deviation of brightness temperatures due to effective radius, as shown by the red curve in Fig. 3 (a), is around 1 K, and the standard deviation due to IWC profile, as shown in Fig. 3 (b), is around 4 K. Therefore, the infrared radiances are more sensitive to the IWC than the effective radius.

It is interesting to note that despite the similarity between the two STD spectra in Figure 3 (a) and (b) in the mid-infrared, there are noticeable differences in the far-infrared channels (wavenumbers smaller than 500 cm^{-1}), suggesting that far-infrared channels, e.g., from future instruments, such as FORUM (https://www.forum-ee9.eu) and TICFIRE (Blanchet et al., 2011), may be advantageous for the UTLS retrieval, which is beyond the scope of this OSSE but warrants future investigations.

Atmospheric
Measurement
Techniques
Discussions
Open Access
EGU

Here, in Fig. 3 (c) we investigate what spectral uncertainties may be caused by the slab-cloud assumption. Similarly,
$R(Re, IWC)$, the radiances corresponding to the effective radius and IWC of individual profiles, are computed for the 100
profiles selected earlier. For each radiance spectrum, we calculate the brightness temperature of a window channel at 1231
cm^{-1}, BT_{1231}. Following the slab-cloud assumption used by Feng and Huang (2018), we then place at the vertical layer where
the atmospheric temperature differs the least from BT_{1231}, a 500-m thick cloud layer with uniform IWC of 1.5 g/m^3. The
temperature of this vertical layer is adjusted to BT_{1231}. With this prescribed cloud layer, radiances are calculated again for each
profile, denoted as $R(Re_0, slab)$; note that the BT_{1231} values of $R(Re, IWC)$ and $R(Re_0, slab)$ are identical. The difference
between $R(Re, IWC)$ and $R(Re_0, slab)$ at other frequencies can be interpreted as radiance residuals not explained by the
slab-cloud assumption. The mean bias and STD of the residuals, as well as the root-mean-square of the residuals (RMSE), are
shown in Fig. 3 (c).

Fig. 3 (c) shows that the slab-cloud assumption cannot fully account for the spectral variations of cloud emission. The
assumption leads to a spectrally tilted mean radiance bias as shown by the blue curve in Fig. 3 (c). The STD of the radiance
residual is of a similar magnitude to the mean bias, suggesting that removing the mean bias would not significantly reduce the
errors in the simulated spectra. The RMSE of $R(Re_0, slab)$ shows minimum errors of around 0.1 K in the mid-infrared window
and maximum errors over 0.5 K in the far-infrared channels. This RMSE spectrum, referred to as ε_{cld}, is also calculated using
an AIRS-like spectral response function to represent the radiance uncertainty induced by slab-cloud assumption in Section 2.3.

2.3 Retrieval Algorithm

The cloud-assisted retrieval proposed by Feng and Huang (2018) is an optimal estimation method (Rodgers, 2000) that retrieves
atmospheric states above clouds using infrared spectral radiances. Similar to Eq.1 in Feng and Huang (2018), we express the
relation between the observation vector, y, and the state vector, x, as follows:

$$y = F(x_0) + \frac{\partial F}{\partial x}(x - x_0) + \varepsilon \qquad (1)$$

$$= y_0 + K(x - x_0) + \varepsilon \qquad (2)$$

Following a similar definition to Feng and Huang (2018), the state vector includes temperature x_t and the logarithm of specific
humidity, x_q, in 67 model layers. x_0 refers to the first guess of the state vector, which is the mean of the *a priori*. y contains
the infrared radiances observation, y_{rad}. F is the forward model that relates x to y. Here, the forward model is the radiative
transfer model, MODTRAN 6.0, configured with the spectral response function of the AIRS instrument. The forward model
can be linearly approximated by the Jacobian matrix K. ε is the residual that includes the measurement error and the forward
model error.

Following the optimal estimation method (Rodgers, 2000, Eq. 5.9), the estimate of x, $\hat{x}$, is expressed as:

$$\hat{x} = x_0 + GK(x - x_0) + G(y - Kx) \qquad (3)$$

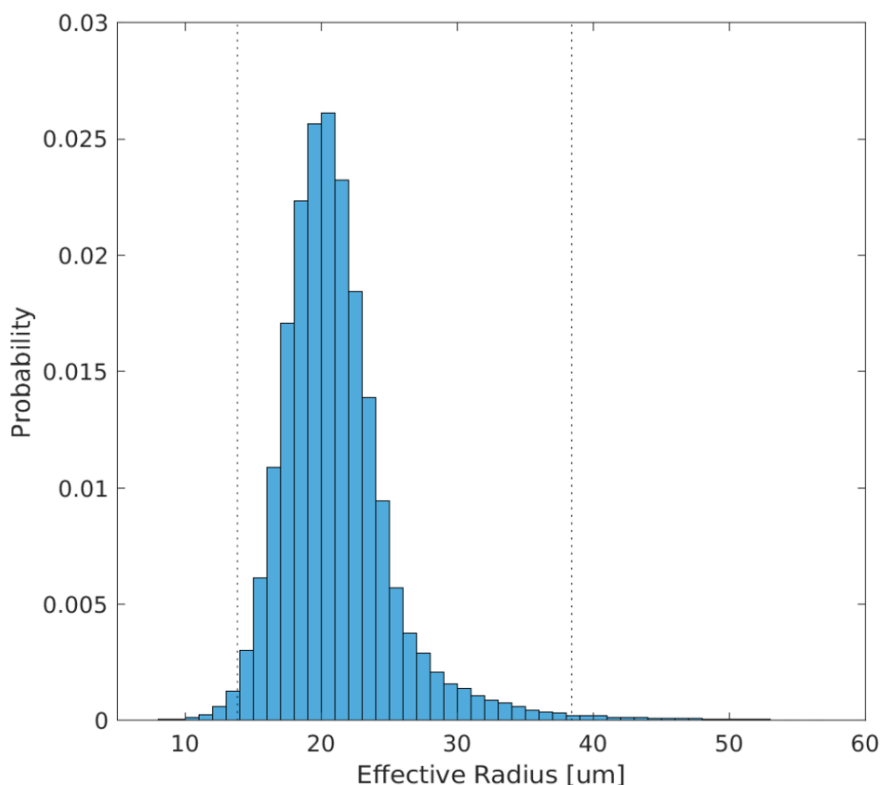$$G = S_a K^T (K S_a K^T + S_\varepsilon)^{-1} \qquad (4)$$

Atmospheric
Measurement
Techniques

Open Access

EGU

Discussions

Figure 2. Histogram of the effective radius (μm) of the cloud ice particles at 100 hPa, based on the samples of 947 tropical cyclone events taken from the DARDAR-cloud dataset. The vertical dotted lines represent 1th and 99th percentiles of the effective radius.

185   Where S_a and S_ε are the covariance matrix of the state vector as given by the *a priori* dataset and that of the error in the observation vector, respectively. S_ε is set to be a diagonal matrix because the observation errors in different channels are considered to be uncorrelated.

     The $\hat{x}$ can then be iteratively solved through:

$$\hat{x}_{i+1} = x_0 + (K_i^T S_\varepsilon^{-1} K_i + S_a^{-1})^{-1} K_i^T S_\varepsilon^{-1} [y - F(\hat{x}_i) + K_i(\hat{x}_i - x_0)] \tag{5}$$

190   Where the subscript i refers to the ith iteration step.

     The equations described above are adopted from Feng and Huang (2018), where the state vector x includes temperature and the logarithm of specific humidity. For comparison, we adopt the slab-cloud retrieval scheme of Feng and Huang (2018) as described above and refer to the result as the slab-cloud retrieval in the following. The only difference to Feng and Huang (2018) is in the prescription of S_ε. While S_ε in Feng and Huang (2018) is the square of NESR (noise equivalent spectral

195 radiances), S_ε in this study for slab-cloud retrieval contains the sum of the square of NESR and the square of ε_{cld}, as depicted in Figure 3, to account for the radiance uncertainties induced by slab-cloud assumption.
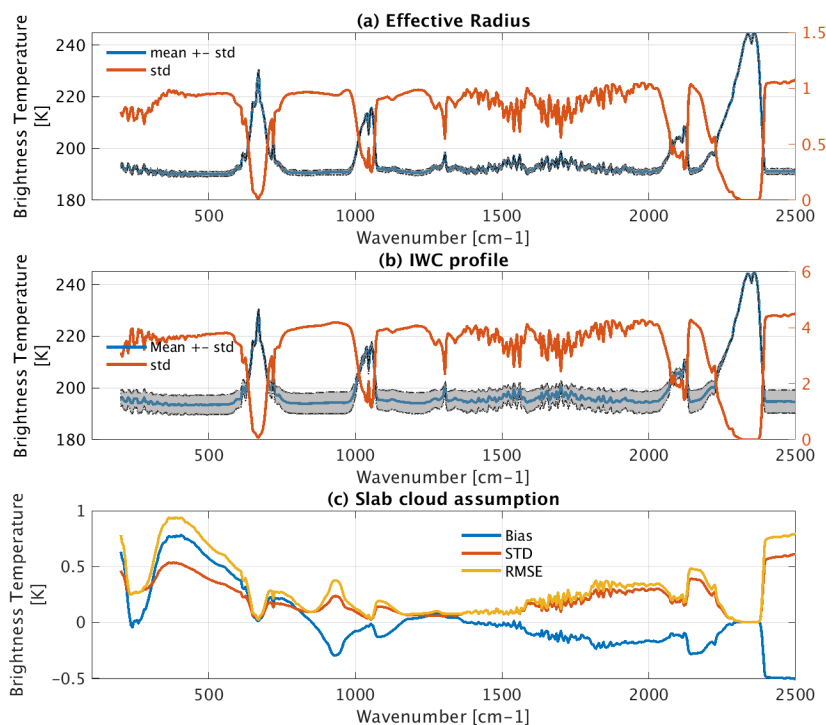
Figure 3. Effect of (a) Effective radius and (b) IWC on the infrared radiance spectrum from 200 to 2700 cm^{-1}.

The blue curves represent the mean of the radiances, $R(Re, IWC_0)$ and $R(Re, IWC_0)$, driven by Re and IWC variations, respectively; the grey areas, as well as the red curves (corresponding to the right y-axis), denote the STD of the radiances. (c) The mean bias, STD, and RMSE of the radiances simulated with the slab-cloud assumption, $R(Re_0, slab)$. The brightness temperature spectra are convolved and presented at a spectral resolution of 5 cm^{-1}.

2.3.1 Synergetic-cloud retrieval

The radiance uncertainty due to the slab-cloud assumption, ε_{cld}, can be largely eliminated by incorporating collocated observations of cloud profile, from active sensors (CloudSat-CALIPSO) along the same track as the hyperspectral infrared sounder

200 (such as AIRS). Instead of simply prescribing the cloud profile from the active sensors in the forward model, motivated by the work of Turner and Blumberg (2018), we include relevant cloud variables in a synergetic retrieval. Turner and Blumberg (2018) demonstrated that the additional observation vector, such as atmospheric and cloud profiles from other instruments and NWP products, can improve the precision of the retrieval and also the convergence in cloudy scenes. Following this idea, the observation vector y in Eq.1 is formulated as: $[y_{rad}, y_{other}]$, where y_{rad} is the infrared radiances observation, and y_{other}

205 includes elements other than radiances observation that we refer to as additional observation vector. Specifically, we include collocated cloud observations, $[y_{iwc}, y_{Re}]$, which mimics those from the DARDAR-cloud product, in the observation vector y
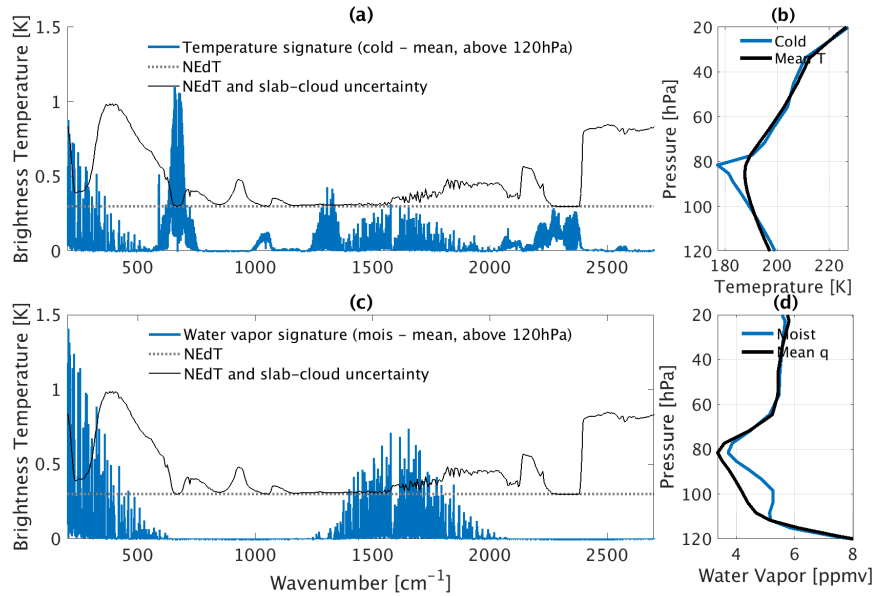
Figure 4. Spectral signals of above-storm atmospheric variations in (a) temperature and (c) water vapor. The signals are obtained by differencing the upwelling radiances at the TOA simulated from the mean profile (black curves in panels b and d) and the radiances simulated from the mean profile of the overshooting convections near the cyclone center (blue curves in panel b and d). These signals are shown in a spectral resolution of 0.1 cm^{-1}. In a and c, the grey dotted lines denote the NEdT of 0.3 K (characterizing the AIRS instrument) and the black solid lines denote the uncertainties combining the NEdT and slab-cloud assumption-induced radiance uncertainty, ε_{cld}, which are convoluted in 5 cm^{-1} spectral intervals

and also add $[x_{iwc}, x_{Re}]$ to the state vector x. At every iteration step (Eq. 5), $[x_{iwc}, x_{Re}]$ is updated along with temperature and humidity profiles. This retrieval method is referred to as the synergetic-cloud retrieval method in the following.

In this OSSE, y_{iwc} is set to be the logarithm of the IWC profile to be consistent with the retrieval of active cloud sensors
210 within the field of view of the infrared sounder. For example, the DARDAR-cloud product provides effective radius and IWC retrieval based on observation from CloudSat and CALIPSO. The uncertainty in IWC measurements is estimated by averaging the posterior uncertainty of IWC, provided by DARDAR-cloud product for every footprint, in the OT-DCC profiles identified in Section 2.2.1. This estimated precision is denoted as ε_{iwc}, which corresponds to an around 20% uncertainty in IWC at vertical levels near the tropopause. Then, we account for the IWC observation uncertainty by randomly perturbing the y_{iwc} so that the
215 y_{iwc} deviates from the truth by an error that has a standard deviation of ε_{iwc}. Similarly, the effective radius observation y_{Re} is obtained by assuming an uncertainty of 5 um. We note that this uncertainty prescription is higher than the typical value in the DARDAR-cloud product (1.6 μm) as we aim to account for sampling differences of the instruments. Because the satellite-measured infrared radiances are most sensitive to cloud emission near the cloud top, we only keep the top 1.5 km of IWC profile in y_{iwc}, which corresponds to six model layers in the radiative transfer calculations.

Atmospheric
Measurement
Techniques
Discussions

Open Access

EGU

220   The diagonal elements of S_ε for y_{iwc} and y_{Re} are then set by conservatively quadrupling the square of the uncertainty ranges of these variables specified above.

    In the state vector, x_{iwc} contains the six layers of the logarithm of IWC at the same model layers as y_{iwc}. Note that x_{iwc} and y_{iwc} are not required to have the same vertical resolution; in practice, the vertical resolution of y_{iwc} can be much finer than model layers. The first guess and covariance matrix of x_{iwc} are calculated using the same *a priori* dataset described in
225 the previous section, although the cross-correlation between IWC and other atmospheric variables is neglected. Consequently, the forward model for relating x_{iwc} to y_{iwc} is a matrix that linearly interpolates the pressure level of x_{iwc} to match the level of y_{iwc}.

2.4   Additional atmospheric observations

    Besides the cloud observations, other products that provide collocated atmospheric profiles can be useful in improving the pre-
230 cision of the posterior estimation. These additional products may include the atmospheric observations from other instruments that are in the same satellite constellation as the hyperspectral infrared sounder or from a NWP model. In this study, we investigate the effect of additional atmospheric observations by adding an observation vector y_{atm}, which contains the temperature and the logarithm of specific humidity at a later time step: 810 minutes after the initial time, in the GEM simulation.

    The distribution of retrieval variable fields is shown in Figure 6. As inferred by the brightness temperature, the massive spatial
235 coverage of DCCs is evident at the time step used as the 'Truth' (410 minutes after the initial time in the GEM simulation). At the later time step (810 minutes), the atmospheric data used as y_{atm} are taken from the same locations but deviate from the 'Truth' as they are not directly above the convective overshoots at this later time step. The RMSE between atmospheric profiles from the two time steps (410 and 810 minutes) defines the uncertainties in y_{atm}. To be conservative, the uncertainty of y_{atm} is set by quadrupling the square of the RMSE in the corresponding diagonal elements of S_ε.

240 ## 3   Results

    Five retrieval cases are designed to assess the retrieval performance of the slab-cloud and synergetic cloud retrieval methods. Among them, Cases 1 and 2 use the slab-cloud retrieval method; Cases 3 and 4 use the synergetic cloud retrieval method that incorporates cloud observations. Cases 2 and 4 differ from Cases 1 and 3 in that they add y_{atm} in the retrieval. The components of state vectors and observation vectors for the four cases are listed in Table 1. Case 5 is added to ascertain the improvements
245 attributable to infrared radiances (as opposed to other sources of information). In this case, we estimate the state vector without using infrared radiances y_{rad} in the synergetic cloud retrieval. Case 5 is relatively uniform in space and it is therefore not included in the figures but listed in Tables 1 and 2 for comparison.

    Before conducting the retrieval experiments, the capability of retrieval methods is investigated 1) by comparing the spectral signal of atmospheric anomalies to the radiance uncertainties, and 2) by calculating the information content for each element
250 of the state vector.

Feng and Huang (2018) demonstrated that the spectral signal of water vapor perturbations emerges above the noise level defined by instrument NEdT. Here, we are interested in whether the atmospheric variations, as simulated by the NWP model and depicted in Figure 1, produce spectral signals that are not obscured by radiance uncertainty due to slab-cloud assumption (ε_{cld}).

255   Figure 1 shows that near the cyclone center (141° E, 16° N), there are strong cooling and hydration above overshooting DCCs. The mean profile of this region is denoted as t_{cold} and q_{mois} for temperature and water vapor, respectively. The spectral signals of water vapor are then obtained by differencing $R(t_0, q_{mois})$ - $R(t_0, q_0)$, where t_0 and q_0 are the mean of the *a priori* dataset. The strength of signals under different spectral specifications was depicted in Feng and Huang (2018) and are not repeated here. The spectral signals are then compared to radiance uncertainties in Figure 4.

260   Figure 4 shows that the radiance uncertainty from the slab-cloud assumption, ε_{cld}, does not completely obscure the signal of temperature or water vapor. In the CO_2 and water vapor channels where the signal mainly comes from, the TOA radiances are not sensitive to cloud emission due to a stronger atmospheric attenuation at these channels. ε_{cld} becomes larger in the wings of absorption channels, where the signals are already masked by the instrument NEdT. Therefore, the information content in temperature and water vapor is not expected to be lost due to the uncertainty caused by the slab-cloud assumption.

265   We next examine the DFS [degree of freedom for signal (Rodgers, 2000)] of temperature and water vapor in the four retrieval cases (Table 1). DFS is defined as the trace of averaging kernel A, which relates the retrieved state $\hat{x}_{i+1}$ to the true state x_0, as derived from Equation 5 at the end of the iteration:

$$\hat{x}_{i+1} - x_0 = A(x - x_0) \tag{6}$$

$$A = (K^T S_\epsilon^{-1} K + S_a^{-1})^{-1} K^T S_\varepsilon^{-1} K \tag{7}$$

270   For a proper comparison, only the infrared radiance observation is included to calculate the DFS, so that a higher DFS indicates higher information content brought by infrared radiances y_{rad}. Because the DFS depends on the cloud distribution, we calculate the average of DFS in the 100-profile test set with individual IWC profiles.

As expected from Figure 4 (a,b), the DFS of temperature and water vapor differ, although not substantially, between Cases 1 and Case 3. The DFS of temperature increases from 3.31 to 4.15 by adopting the synergetic-cloud method owing to the

275   improved sounding near the cloud top, where sparse ice cloud particles do not fully attenuate the atmospheric emission. In comparison, the slab-cloud retrieval method fails to capitalize the information near the cloud top, as it neglects the contributions to satellite radiances from the vertical layers around the assumed sharp cloud boundary. Therefore, the synergetic retrieval method is expected to achieve a better result in temperature.

Moreover, a significant DFS of IWC (1.93 out of 6, on average) is found. The DFS suggests the sensitivity of infrared

280   radiances to the IWC profile near the cloud top, which is consistent with the large spectral variations caused by perturbation in the IWC profile simulated from the DARDAR-cloud product (Figure 4 (b)). Hence, the retrieval method can improve the precision in IWC products provided by collocated cloud observations. Note that the DFS for IWC varies from 0.96 to 2.71 in the test set, depending on the optical depth near the cloud top. Low ice density near the cloud top leads to higher DFS of IWC. For example, the DFS in IWC increases from 0.99 to 2.44 in Figure 7 (f) compared to Figure 7 (c). On the other hand, the DFS

Table 1. State vector and observational vector of four cases of simulation experiments.

	x	y	DFS
		Slab-cloud	
Case 1	x_t, x_q	y_{rad}	t: 3.31/20, q: 0.88/20
Case 2	x_t, x_q	y_{rad}, y_{atm}	Same as Case 1
		Synergetic-cloud	
Case 3	$x_t, x_q, x_{iwc}, x_{Re}$	y_{rad}, y_{iwc}, y_{Re}	t: 4.15/20, q :0.93/20, IWC :1.93/6, Re: 0.01/1
Case 4	$x_t, x_q, x_{iwc}, x_{Re}$	$y_{rad}, y_{atm}, y_{iwc}, y_{Re}$	same as Case 3
Case 5	$x_t, x_q, x_{iwc}, x_{Re}$	y_{atm}, y_{iwc}, y_{Re}	\

Table 2. Performance assessments of four cases of simulation experiments.

	t [K] at 81 hPa		q [ppmv] at 81 hPa		CIWV [g/m^2] from 110 to 70 hPa		IWC [g/m^3] at 90 hPa	
	Bias	RMSE	Bias	RMSE	Bias	RMSE	Bias	RMSE
prior	6.8	7.1	-1.8	1.5	-0.30	0.34	-0.0014	0.0237
$[y_{atm}, y_{iwc}]$	7.7	10.4	-1.7	2.3	-0.17	0.24	-0.0049	0.0094
					Slab-cloud			
Case 1	-0.1	4.5	-1.8	2.4	-0.28	0.37	\	\
Case 2	0.8	4.1	-0.6	1.0	-0.11	0.16	\	\
					Synergetic-cloud			
Case 3	-0.2	3.5	-1.7	2.2	-0.2	0.30	0.0028	0.0051
Case 4	0.8	2.7	-0.8	1.1	-0.09	0.16	0.0028	0.0051
Case 5	2.7	4.9	-1.5	2.0	-0.15	0.25	-0.0041	0.0089

285 in effective radius is very limited (0.01). It can be expected from Figure 3 (a,b) which shows that effective radius has a smaller impact on infrared radiances compared to IWC.

In the following, retrieval is performed for the 100 profiles in the test set using Eq. 5 and following the OSSE framework described above. We then evaluate the retrieval performance through the mean bias and RMSE in temperature, humidity, and IWC between the retrieved profiles and the truth, as shown in Figure 5. The retrieval performance is also evaluated with regard

290 to these quantities at selected levels and with regard to CIWV integrated from 110 to 70 hPa.

Atmospheric
Measurement
Techniques
Discussions

Open Access

EGU

3.1 Slab-cloud retrieval

To recap, Cases 1 and 2 use the slab-cloud retrieval method. Improving upon Feng and Huang (2018), Case 1 accounts for the radiance uncertainties due to the slab-cloud assumption, while Case 2 further incorporates additional atmospheric observations to improve the precision of the method.

295   The results of Case 1 are shown in red solid curves in Figures 5 and 7. The major improvement in Case 1, compared to the prior (blue solid curves), is the temperature profile from 100 to 75 hPa. Although there are some DFS values for water vapor, Case 1 does not improve much from the first guess.

     Case 2 improves from Case 1 owing to the information carried by the additional atmospheric observation, y_{atm}. Case 2 is represented by the red dotted curves in Figures 5 and 7. It approaches the truth more than Case 1, despite the warm/dry biases

300   in the first guess and y_{atm} (See Figure 5 (a,c)). Noticeably, it increases the retrieved water vapor concentration by around 1 ppmv on average and reduces the RMSE from 2.4 ppmv to 1.0 ppmv, as shown in Figure 5 (c,d) and Table 2. For the CIWV, Case 2 reduces the RMSE by half, compared to Case 1.

     To demonstrate how well the retrieved atmospheric field represents the spatial variability in the truth, namely a moister and colder UTLS region above the cyclone center as shown in Figure 1, the distributions of water vapor, temperature, and CIWV

305   are presented in Figure 6. It shows that the 'true' spatial patterns are well reproduced by Case 2 retrieval.

     Furthermore, individual profiles from two clusters of overshooting DCCs, which includes the DCCs near the cyclone center and those in the south of the domain, are randomly selected to investigate how well the retrieval reproduces the vertical variability in temperature and water vapor. The all-sky optical depth from TOA, along with the IWC profile, at the two locations is shown in Figure 7 (c,d). Less than 13.5% of the atmospheric emission transmits to the TOA is from layers where all-sky

310   optical depth is higher than 2. Therefore, the retrievable radiative signals come from the atmospheric column above thick cloud layers, i.e., where optical depth is less than 2.

     Figure 7 (a-c) shows the results in a location close to the cyclone center. At this location, the slab-cloud method prescribes the cloud layer at the cold-point due to the strong cloud emission. Atmospheric anomalies above 86 hPa have an impact on TOA infrared radiances. Around 80 hPa, the truth profile that we aim to retrieve is around 8 K colder than the prior and nearly

315   3 ppmv moister. While the result from Case 1 overcomes the bias in temperature, it produces moistening in a board vertical range which, as explained in Feng and Huang (2018), is due to the strong smoothing (smearing) effect of the averaging kernel in this case. In comparison, Case 2 correctly produces a peak moistening around 80 hPa, while keeping its temperature profile similar to Case 1.

     Figure 7 (d-f) shows the results in a location south of the domain, where the slab-cloud method prescribes the cloud layer

320   at 95 hPa. At this location, the cloud emission from the top 1.5 km cloud layer affects infrared radiances strongly, which can be inferred from the optical depth (Figure 7 (f)), leading to a large radiance residual that cannot be explained by slab-cloud assumption. Therefore, Case 1 fails to improve upon the prior. Case 2 leads to a moister posterior compared to the prior owing to the addition of y_{atm}. However, Case 2 fails to update the temperature profile above the cloud layer. Instead, it approaches the y_{atm} in lower altitudes that lead to unrealistic vertical oscillation in temperature near 100 hPa.

Atmospheric
Measurement
Techniques
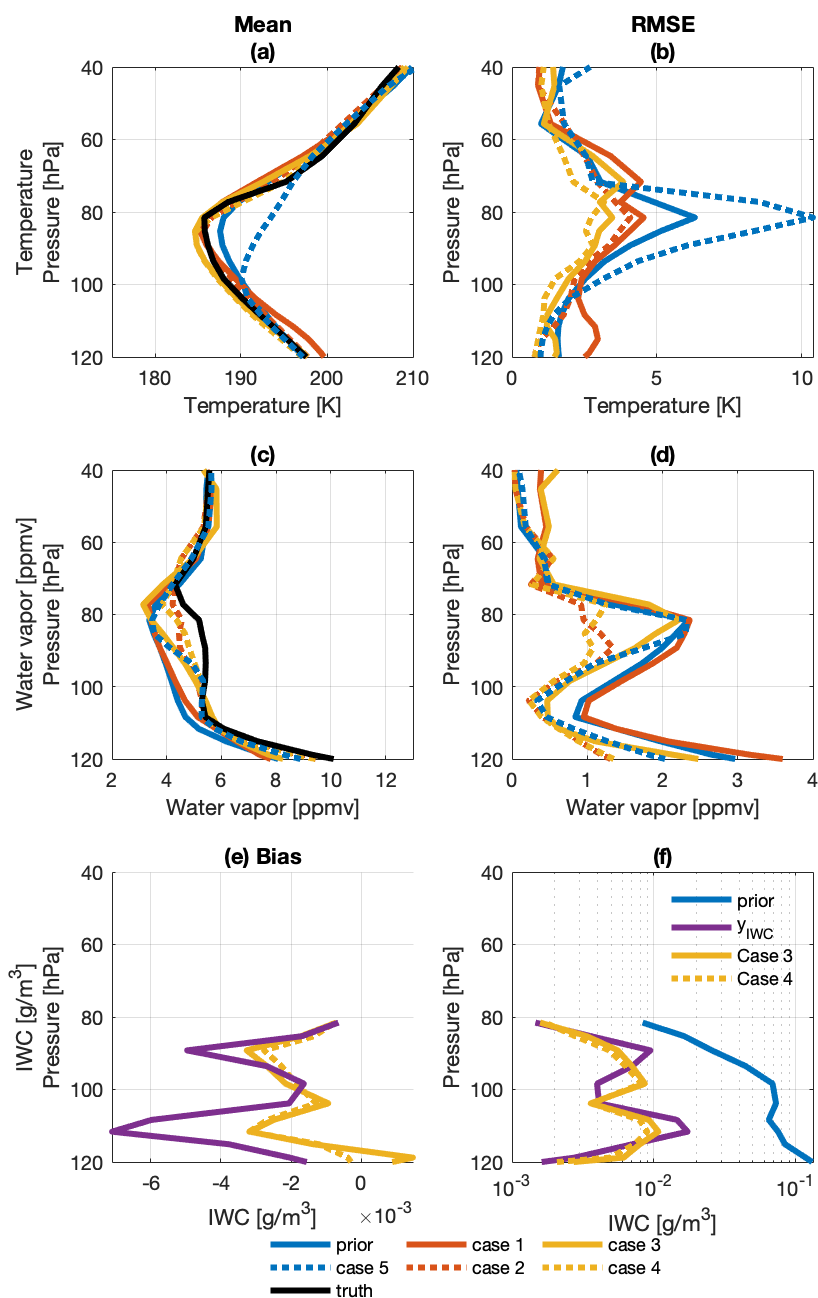Discussions

Open Access

EGU

Figure 5. Mean and RMSE of temperature (a,b), water vapor (c,d) profiles from the four cases of the retrieval simulation experiments. Bias (e) and RMSE (f) of IWC profiles. Blue curves show the bias and RMSE in the prior. Retrieval cases using the slab-cloud method are marked in the solid curve (case 1 in red and case 2 in orange), while the retrievals using the synergetic-cloud method are marked in the dotted curve (case 2 in red and case 4 in orange).
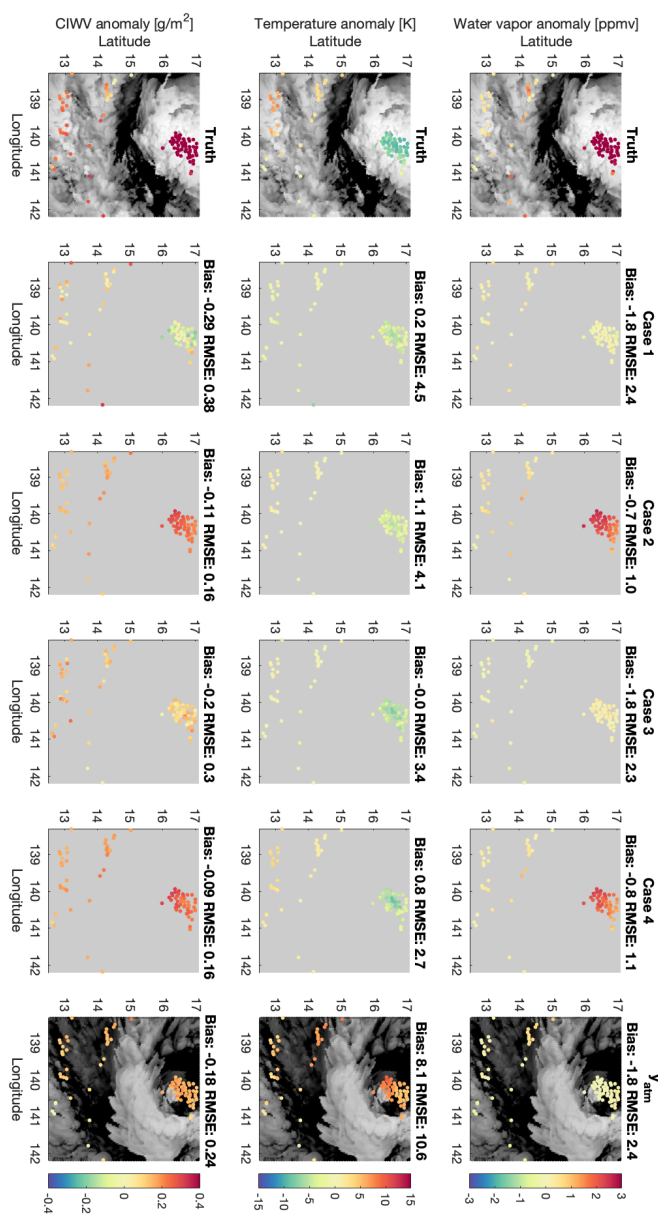
Atmospheric
Measurement
Techniques
Discussions
Open Access

EGU

Figure 6. Horizontal distributions of the anomalies, defined as the deviation from x_0, in water vapor (in the units of ppmv, upper panels), temperature (in the units of K, middle panels) at 81 hPa, and column integrated water vapor between 110 and 70 hPa (in the units of g/m^2, lower panels). The truth fields are shown in the first column, with its background grey-shaded for BT_{1231}. The second to fifth columns show retrieved results from the four cases of simulation experiments described in Table 1. The fifth column show distribution of the additional observation vector, y_{atm}, incorporated in the retrievals of Cases 2 and 4. This additional atmospheric observation y_{atm} is taken from 810 minutes after the initial simulation time step.
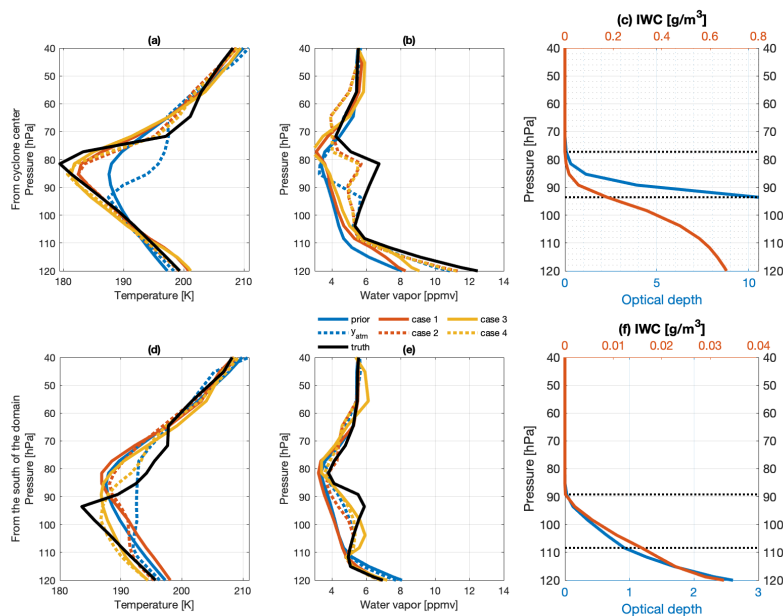
Atmospheric
Measurement
Techniques

Discussions

Figure 7. (a,d) Temperature and (b,e) water vapor profiles of first guess (blue solid) and truth (black solid) and the posterior (red and yellow curves represent the slab-cloud and synergetic-cloud retrieval method, respectively, while the solid curves are cases without y_{atm} and dotted curves include y_{atm}), for two profiles from the test set. (c,f) IWC (red curve, corresponding to the upper x-axis) and all-sky optical depth from the TOA (blue curve, corresponding to the lower x-axis) of two selected profiles. Dotted black lines mark the vertical range of ice clouds included in the y_{iwc} and x_{iwc}, while ice clouds in the lower vertical levels are prescribed to be the same as the cloud observation.

3.2 Synergetic-cloud retrieval

Using the synergetic-cloud retrieval method, Case 3 becomes more sensitive to water vapor and temperature compared to Case 1, as indicated by the reduced RMSE in Table 2 and the better resemblance of the truth in Figure 6. It retrieves higher water vapor concentration from 110 to 70 hPa, in comparison with Case 1. Owing to the radiative emission from in-cloud layers between 110 to 95 hPa, Cases 3 and 4 become sensitive to temperature profile near the cloud top. Hence, Cases 3 and 4 reduce the RMSE compared to other cases.

The advantage of the synergetic retrieval method, especially when IWC near the cloud top is relatively small, is illustrated in Figure 7 (d-f). At this location, the radiative signal from the moistening near the cloud top can be transmitted to the TOA. As a result, Case 3 produces the enhanced water vapor in Figure 7 (e) and approaches the truth cloud-top temperature much better than Cases 1 and 2. Case 4 further benefits from y_{atm} which constrains the profile in the vertical ranges below 110 hPa and above 80 hPa. Case 4 reproduces the oscillating temperature feature in Figure 7 (d), correcting the warm bias found in both y_{atm} and the first guess around 90 hPa.

Atmospheric
Measurement
Techniques
Discussions

Open Access

EGU

In addition, Figure 5 (e,f) shows that the synergetic retrieval method can improve upon the collocated cloud observations by reducing the mean biases in the IWC profile. At 90 hPa, where the retrieved 1.5 km cloud layer overlaps the most between the test set, the retrieval reduces the RMSE and mean biases in the y_{iwc} by half. This can be beneficial considering the sampling

340   difference between the active sensor and infrared instruments.

While the improvement in Cases 2 and 4 shows the advantage of including additional atmospheric products, y_{atm}, one caveat is in the proper evaluation of the uncertainty range, which is included in the covariance matrix of the observation vector. This is important as the uncertainty range in y_{atm} constrain the posterior uncertainty range of the retrieval at each vertical level. In this study, we account for the difficulties in evaluating S_ε by increasing the RMSE in the y_{atm}, so that the square root of S_ε of

345   y_{atm} is equivalent to a doubling of RMSE shown in Figure 5 (b,d) blue dot line.

Although the additional measurement vector, y_{atm}, itself does not contain the spatial variability pattern as seen in Figure 6, the corresponding covariance in S_ε properly accounts for its variability (uncertainty) by prescribing a large value around 80 hPa but smaller values at other vertical ranges. Therefore, it increases the confidence to the posterior at levels where the thermodynamic variables are relatively constant. The increased confidence in turn enhances the degree of freedom in the

350   ranges around 80 hPa, where the warm and dry signals mainly come from. Therefore, even though y_{atm} itself deviates from the truth, including y_{atm} in optimal estimation can still improve the posterior estimation. In reality, the uncertainty in available atmospheric products can be estimated by inflating the precision of the product to account for sampling size differences through comparison with NWP models and collocated observations.

4   Conclusion and Discussion

355   Sounding the UTLS thermodynamical conditions has been a challenge. Using simulation experiments, we aim to understand whether the variability in temperature and humidity field, especially above convective storms, can be detected by hyperspectral infrared sounders. Our focus is to investigate and constrain the uncertainties induced by clouds. Two retrieval schemes are tested, including a slab-cloud scheme that uses mainly the infrared radiance measurements and a synergic cloud retrieval scheme that combines cloud observations from collocated active sensors.

360   First, we find that uncertainties in cloud properties near the top of overshooting deep convective clouds have a non-negligible impact on the TOA infrared radiances (Figure 3). The variation in brightness temperature of the TOA radiances due to vertical distribution of IWC may amount to about 4 K. It is the largest in window channels and weak absorption channels which are sensitive to cloud emission. Adopting a slab-cloud assumption, which locates a clear-cut cloud top using the brightness temperature of the window channel, alleviates, but does not fully eliminate, the cloud effect on the radiance spectrum (Figure 3

365   (c)). This remaining radiance uncertainty is accounted for in this study and is found to not significantly obscure the temperature and humidity signals in the retrieval. Therefore, it is affirmed that the cloud-assisted retrieval as proposed by Feng and Huang (2018), can improve the sounding of UTLS temperature and water vapor compared to the prior knowledge. However, this retrieval neglects information content from the in-cloud atmosphere. As a result, it may lead to biases in individual temperature

profiles. For example, as shown in Figure 7 (c), the slab-cloud retrieval fails to reproduce the oscillating temperature anomalies,

370   although it still detects the moistening water vapor anomalies above convective storms.

Second, we find that the synergetic-cloud retrieval method, especially after incorporating additional atmospheric observations y_{atm}, is sensitive to temperature, water vapor, and also IWC profile, near and above the cloud top. It substantially reduces the RMSE in temperature from 7.1 to 2.7 K compared to the prior. It also reduces the RMSE in column integrated water vapor by half. It is capable of producing the strong moistening feature of the individual profile (as shown by Figure 7 (b)) and detect-

375   ing the oscillating temperature anomalies (as shown by Figure 7 (c)). The retrieved distributions of temperature and humidity also best resemble the horizontal distribution patterns in the truth at a fixed pressure level (Figure 6).

In conclusion, the OSSEs here suggest that it is promising to apply the synergetic-retrieval method, using the infrared hyperspectra and cloud profiles from the existing instruments: AIRS, CloudSat, and CALIPSO, to retrieve the UTLS temperature and water vapor above the deep convective clouds. One suitable application is the tropical cyclone events which generate massive

380   upper tropospheric thick clouds that provide a favorable condition for the retrieval technique developed here, which we will address in an accompanying paper (Feng and Huang., 2021). Although not explicitly discussed in this study, similar results shown in Figures 5 to 7 can be obtained using other hyperspectral infrared sounders, e.g., IASI and CrIS, due to their similar spectral specifications to AIRS. As discussed in Feng and Huang (2018), the sensitivity to water vapor and cloud microphysics properties (see Section 2.2.1) can be further improved by including a far-infrared coverage provided by future instruments, .e.g.,

385   FORUM and TICFIRE. While a limited number of samples is available for the synergetic retrieval to perform, instruments in geostationary orbit, such as IRS (Infrared Spectrometer) and GIIRS (Geostationary Interferometric Infrared Sounder) (Schmit et al., 2009; Holmlund et al., 2021), can greatly increase the collocation with other spaceborne active sensors over convective region. It may also benefit the understanding of convective impacts by providing time-continuous observations (Li et al., 2018) in future research. The ability of the synergetic retrieval method in using hyperspectral infrared observations to improve the

390   NWP outputs (y_{NWP}) also suggests the advantage of including cloudy-sky observations in the global data assimilation system as performed in Okamoto et al. (2020).

Data availability.   Derived data supporting the findings of this study are available from JF on request. The data for assessing cloud-induced uncertainties is openly available at http://dx.doi.org/10.17632/fy3gg7ch42.1.

Author contributions.   YH conceived the cloud-assisted retrieval idea; JF implemented this idea with improvements using the synergetic-

395   retrieval method. ZQ carried out the NWP simulation. JF and YH co-designed the OSSE and wrote this paper with contributions from ZQ.

Competing interests.   The authors declare that they have no conflict of interest.

References

Anderson, J. G., Wilmouth, D. M., Smith, J. B., and Sayres, D. S.: UV dosage levels in summer: Increased risk of ozone loss from convectively
405   injected water vapor, Science, 337, 835–839, 2012.

Aumann, H. and Ruzmaikin, A.: Frequency of deep convective clouds in the tropical zone from 10 years of AIRS data, Atmospheric
Chemistry and Physics, 13, 10 795–10 806, 2013.

Bani Shahabadi, M., Huang, Y., Garand, L., Heilliette, S., and Yang, P.: Validation of a weather forecast model at radiance level against
satellite observations allowing quantification of temperature, humidity, and cloud-related biases, Journal of Advances in Modeling Earth
410   Systems, 8, 1453–1467, 2016.

Baum, B. A., Yang, P., Heymsfield, A. J., Schmitt, C. G., Xie, Y., Bansemer, A., Hu, Y.-X., and Zhang, Z.: Improvements in shortwave bulk
scattering and absorption models for the remote sensing of ice clouds, Journal of Applied Meteorology and Climatology, 50, 1037–1056,
2011.

Bélair, S., Mailhot, J., Girard, C., and Vaillancourt, P.: Boundary layer and shallow cumulus clouds in a medium-range forecast of a large-
415   scale weather system, Monthly weather review, 133, 1938–1960, 2005.

Berk, A. and Hawes, F.: Validation of MODTRAN® 6 and its line-by-line algorithm, Journal of Quantitative Spectroscopy and Radiative
Transfer, 203, 542–556, 2017.

Berk, A., Conforti, P., Kennett, R., Perkins, T., Hawes, F., and Van Den Bosch, J.: MODTRAN® 6: A major upgrade of the MODTRAN® ra-
diative transfer code, in: 2014 6th Workshop on Hyperspectral Image and Signal Processing: Evolution in Remote Sensing (WHISPERS),
420   pp. 1–4, IEEE, 2014.

Biondi, R., Randel, W., Ho, S.-P., Neubert, T., and Syndergaard, S.: Thermal structure of intense convective clouds derived from GPS radio
occultations, Atmospheric Chemistry and Physics, 12, 5309–5318, 2012.

Blanchet, J.-P., Royer, A., Châteauneuf, F., Bouzid, Y., Blanchard, Y., Hamel, J.-F., de Lafontaine, J., Gauthier, P., O'Neill, N. T., Pancrati,
O., et al.: TICFIRE: a far infrared payload to monitor the evolution of thin ice clouds, in: Sensors, Systems, and Next-Generation Satellites
425   XV, vol. 8176, p. 81761K, International Society for Optics and Photonics, 2011.

Bloom, H. J.: The Cross-track Infrared Sounder (CrIS): a sensor for operational meteorological remote sensing, in: IGARSS 2001. Scanning
the Present and Resolving the Future. Proceedings. IEEE 2001 International Geoscience and Remote Sensing Symposium (Cat. No.
01CH37217), vol. 3, pp. 1341–1343, IEEE, 2001.

Blumstein, D., Chalon, G., Carlier, T., Buil, C., Hebert, P., Maciaszek, T., Ponce, G., Phulpin, T., Tournier, B., Simeoni, D., et al.: IASI instru-
430   ment: Technical overview and measured performances, in: Infrared Spaceborne Remote Sensing XII, vol. 5543, pp. 196–207, International
Society for Optics and Photonics, 2004.

Chahine, M. T., Pagano, T. S., Aumann, H. H., Atlas, R., et al.: AIRS: Improving weather forecasting and providing new data on greenhouse
gases, Bulletin of the American Meteorological Society, 87, 911, 2006.

Côté, J., Gravel, S., Méthot, A., Patoine, A., Roch, M., and Staniforth, A.: The operational CMC–MRB global environmental multiscale
435   (GEM) model. Part I: Design considerations and formulation, Monthly Weather Review, 126, 1373–1395, 1998.

Delanoë, J. and Hogan, R. J.: A variational scheme for retrieving ice cloud properties from combined radar, lidar, and infrared radiometer,
Journal of Geophysical Research: Atmospheres, 113, 2008.

Delanoë, J. and Hogan, R. J.: Combined CloudSat-CALIPSO-MODIS retrievals of the properties of ice clouds, Journal of Geophysical
Research: Atmospheres, 115, 2010.

440   DeSouza-Machado, S., Strow, L. L., Tangborn, A., Huang, X., Chen, X., Liu, X., Wu, W., and Yang, Q.: Single-footprint retrievals for AIRS
        using a fast TwoSlab cloud-representation model and the SARTA all-sky infrared radiative transfer algorithm, Atmospheric Measurement
        Techniques, 11, 2018.

Dessler, A., Schoeberl, M., Wang, T., Davis, S., and Rosenlof, K.: Stratospheric water vapor feedback, Proceedings of the National Academy
        of Sciences, 110, 18 087–18 091, 2013.

445   Feng, J. and Huang, Y.: Cloud-Assisted Retrieval of Lower-Stratospheric Water Vapor from Nadir-View Satellite Measurements, Journal of
        Atmospheric and Oceanic Technology, 35, 541–553, 2018.

Gambacorta, A., Barnet, C., Wolf, W., King, T., Nalli, N., Wilson, M., Soulliard, L., Zang, K., Xiong, X., and Goldberg, M.: The NOAA op-
        erational hyper spectral retrieval algorithm: a cross-comparison among the CrIS, IASI and AIRS processing system, in: 19th International
        TOVS Study Conference, Jeju Island, Korea, 2014.

450   Girard, C., Plante, A., Desgagné, M., McTaggart-Cowan, R., Côté, J., Charron, M., Gravel, S., Lee, V., Patoine, A., Qaddouri, A., et al.:
        Staggered vertical discretization of the Canadian Environmental Multiscale (GEM) model using a coordinate of the log-hydrostatic-
        pressure type, Monthly Weather Review, 142, 1183–1196, 2014.

Heymsfield, A. J.: Ice particles observed in a cirriform cloud at- 83 C and implications for polar stratospheric clouds, Journal of the atmo-
        spheric sciences, 43, 851–855, 1986.

455   Holmlund, K., Grandell, J., Schmetz, J., Stuhlmann, R., Bojkov, B., Munro, R., Lekouara, M., Coppens, D., Viticchie, B., August, T., et al.:
        METEOSAT THIRD GENERATION (MTG): Continuation and Innovation of Observations from Geostationary Orbit, Bulletin of the
        American Meteorological Society, pp. 1–71, 2021.

Huang, Y., Leroy, S. S., and Anderson, J. G.: Determining longwave forcing and feedback using infrared spectra and GNSS radio occultation,
        Journal of climate, 23, 6027–6035, 2010.

460   Jiang, B., Lin, W., Hu, C., and Wu, Y.: Tropical cyclones impact on tropopause and the lower stratosphere vapour based on satellite data,
        Atmospheric Science Letters, p. e1006, 2020.

Kirk-Davidoff, D. B., Hintsa, E. J., Anderson, J. G., and Keith, D. W.: The effect of climate change on ozone depletion through changes in
        stratospheric water vapour, Nature, 402, 399–401, 1999.

Li, Z., Li, J., Wang, P., Lim, A., Li, J., Schmit, T. J., Atlas, R., Boukabara, S.-A., and Hoffman, R. N.: Value-added impact of geostationary
465   hyperspectral infrared sounders on local severe storm forecasts—Via a quick regional OSSE, Advances in Atmospheric Sciences, 35,
        1217–1230, 2018.

McClatchey, R. A.: Optical properties of the atmosphere, 411, Air Force Cambridge Research Laboratories, Office of Aerospace Research . . . ,
        1972.

Milbrandt, J. and Yau, M.: A multimoment bulk microphysics parameterization. Part I: Analysis of the role of the spectral shape parameter,
470   Journal of the atmospheric sciences, 62, 3051–3064, 2005.

Okamoto, K., Owada, H., Fujita, T., Kazumori, M., Otsuka, M., Seko, H., Ota, Y., Uekiyo, N., Ishimoto, H., Hayashi, M., et al.: Assessment
        of the potential impact of a hyperspectral infrared sounder on the Himawari follow-on geostationary satellite, SOLA, 2020.

Qu, Z., Huang, Y., Vaillancourt, P. A., Cole, J. N., Milbrandt, J. A., Yau, M.-K., Walker, K., and de Grandpré, J.: Simulation of convective
        moistening of the extratropical lower stratosphere using a numerical weather prediction model., Atmospheric Chemistry & Physics, 20,
475   2020.

Randel, W. and Park, M.: Diagnosing observed stratospheric water vapor relationships to the cold point tropical tropopause, Journal of
        Geophysical Research: Atmospheres, 124, 7018–7033, 2019.

Randel, W. J., Zhang, K., and Fu, R.: What controls stratospheric water vapor in the NH summer monsoon regions?, Journal of Geophysical Research: Atmospheres, 120, 7988–8001, 2015.

480 Rodgers, C. D.: Inverse methods for atmospheric sounding: theory and practice, World Scientific Publishing, 2000.

Schmit, T. J., Li, J., Ackerman, S. A., and Gurka, J. J.: High-spectral-and high-temporal-resolution infrared measurements from geostationary orbit, Journal of Atmospheric and Oceanic Technology, 26, 2273–2292, 2009.

Shindell, D. T.: Climate and ozone response to increased stratospheric water vapor, Geophysical Research Letters, 28, 1551–1554, 2001.

Solomon, S., Rosenlof, K. H., Portmann, R. W., Daniel, J. S., Davis, S. M., Sanford, T. J., and Plattner, G.-K.: Contributions of stratospheric
485 water vapor to decadal changes in the rate of global warming, Science, 327, 1219–1223, 2010.

Stephens, G. L., Vane, D. G., Boain, R. J., Mace, G. G., Sassen, K., Wang, Z., Illingworth, A. J., O'connor, E. J., Rossow, W. B., Durden, S. L., et al.: The CloudSat mission and the A-Train: A new dimension of space-based observations of clouds and precipitation, Bulletin of the American Meteorological Society, 83, 1771–1790, 2002.

Sun, Y. and Huang, Y.: An examination of convective moistening of the lower stratosphere using satellite data, Earth and Space Science, 2,
490 320–330, 2015.

Susskind, J., Barnet, C. D., and Blaisdell, J. M.: Retrieval of atmospheric and surface parameters from AIRS/AMSU/HSB data in the presence of clouds, IEEE Transactions on Geoscience and Remote Sensing, 41, 390–409, 2003.

Tourville, N., Stephens, G., DeMaria, M., and Vane, D.: Remote sensing of tropical cyclones: Observations from CloudSat and A-Train profilers, Bulletin of the American Meteorological Society, 96, 609–622, 2015.

495 Turner, D. D. and Blumberg, W. G.: Improvements to the AERIoe thermodynamic profile retrieval algorithm, IEEE Journal of Selected Topics in Applied Earth Observations and Remote Sensing, 12, 1339–1354, 2018.

Wang, X. and Jiang, H.: A 13-year global climatology of tropical cyclone warm-core structures from AIRS data, Monthly Weather Review, 147, 773–790, 2019.

Werner, F., Schwartz, M., Livesey, N., Read, W., and Santee, M.: Extreme outliers in lower stratospheric water vapor over North America
500 observed by MLS: Relation to overshooting convection diagnosed from colocated Aqua-MODIS data, Geophysical Research Letters, p. e2020GL090131, 2020.

Winker, D. M., Pelon, J. R., and McCormick, M. P.: CALIPSO mission: spaceborne lidar for observation of aerosols and clouds, in: Lidar Remote Sensing for Industry and Environment Monitoring III, vol. 4893, pp. 1–11, International Society for Optics and Photonics, 2003.

Yang, P., Bi, L., Baum, B. A., Liou, K.-N., Kattawar, G. W., Mishchenko, M. I., and Cole, B.: Spectrally consistent scattering, absorption,
505 and polarization properties of atmospheric ice crystals at wavelengths from 0.2 to 100 μ m, Journal of the Atmospheric Sciences, 70, 330–347, 2013.

Yu, W., Dessler, A. E., Park, M., and Jensen, E. J.: Influence of convection on stratospheric water vapor in the North American monsoon region, Atmospheric Chemistry and Physics, 20, 12 153–12 161, 2020.

Zhou, D. K., Smith Sr, W. L., Liu, X., Larar, A. M., Huang, H.-L. A., Li, J., McGill, M. J., and Mango, S. A.: Thermodynamic and cloud
510 parameter retrieval using infrared spectral data, Geophysical research letters, 32, 2005.